First Observation of Quantum Splitting Behavior in Nanocrystalline $SrAl_{12}O_{19}$:Pr, Mg Phosphor

Sergio M. Loureiro,* Anant Setlur, William Heward, Seth T. Taylor, Holly Comanzo, Mohan Manoharan, and Alok Srivastava

General Electric, Global Research Center, 1, Research Circle, Niskayuna, New York 12309, USA

Paul Schmidt and Uwe Happek

Department of Physics and Astronomy, The University of Georgia, Athens, Georgia 30602, USA

Received February 21, 2005. Revised Manuscript Received April 11, 2005

We report on the first observation of quantum splitting effect in nanocrystalline powders of $SrAl_{12}O_{19}$:1% Pr, Mg. The nanocrystalline materials were prepared using a surfactant-templated-assisted route yielding high-quality hexagonal nanocrystallites with thicknesses comprised between 30 and 60 nm. Comprehensive optical studies, including emission, photoexcitation, and time-resolved fluorescence measurements, demonstrate that no physical property degradation such as surface-induced loss mechanisms are found and that the quantum splitting properties of the material are fully retained in the nanocrystalline particles.

Introduction

Luminescent materials play an important role in the lighting industry,[1] especially in fluorescent lamps, where UV radiation from Hg ($\lambda = 185$ or 254 nm) or Xe ($\lambda = 172$ nm) discharges is absorbed by phosphor coatings and down converted into visible radiation. The quantum efficiency (QE) for the down conversion of UV radiation into visible radiation is greater than 0.8 but less than unity.[2] This places an upper bound on the overall efficiency of the fluorescent lamp system since the QE of these phosphors cannot exceed unity. Therefore, the development of phosphors that have visible quantum efficiencies greater than unity under Hg or Xe discharges, otherwise known as quantum-splitting phosphors (QSPs), could enable fluorescent lamp and plasma based display systems with much higher efficiencies.[3]

The process of QS can be described using Figure 1, which shows the electronic structure of the Pr^{3+} ion. Incident VUV photons are absorbed by Pr^{3+} from its ground state ($^3H_4$) into the $4f^15d^1$ configuration. When the lowest 4f5d levels are above the Pr^{3+} $^1S_0$ state, the excitation decays to the $^1S_0$ state situated at ∼46 500 cm^{-1}. Emission from the $^1S_0$ state to the $^1I_6$ level (405 nm radiation) results in the first photon of the QS process. A second transition that connects the upper $^3P_0$ state with several ground-state levels yields the second photon (480−700 nm). However, if the lowest Pr^{3+} $4f^2 \rightarrow 4f5d$ levels are below the $^1S_0$ state, the emission after VUV excitation will be dominated by $4f5d \rightarrow 4f^2$ transitions in the UV spectral region below 300 nm, and the QE in the visible spectral region cannot exceed unity.[4,5] The first demonstration that Pr^{3+}-doped hosts can have QEs exceeding unity was simultaneously reported by Piper et al.[6] and Sommerdijk et al.[7,8] for YF_3:Pr^{3+}, for which a QE of ∼140% was measured

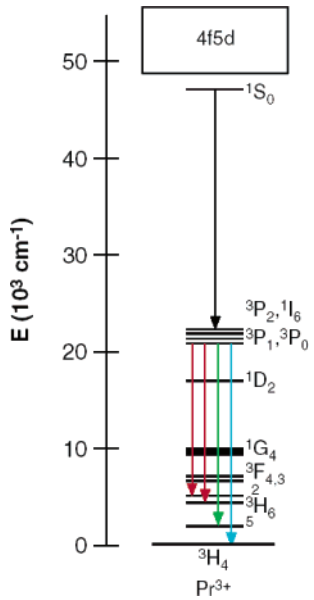

Figure 1. Energy-level diagram for Pr^{3+} ion.

* To whom correspondence should be addressed. E-mail: loureiro@research.ge.com.

(1) Blasse, G.; Grabmeier, B. C. *Luminescent Materials*; Springer-Verlag 1994.
(2) Feldmann, C.; Justel, T.; Ronda, C. R.; Schmidt, P. J. *Adv. Funct. Mater.* **2003**, *13*, 511.
(3) Recent developments in quantum splitting phosphors have been reviewed by: Srivastava, A. M. *Encyclopedia of Physical Science and technology*, 3rd ed.; Academic Press: 2002; Vol. 11, p 855. Srivastava, A. M. *Handbook of Luminescence, Display Materials, and Devices*; Nalwa, H. S., Rowher, L. S., Eds.; American Scientific Publishers: 2003; Vol 3, p 79.
(4) Yang, K. H.; DeLuca, J. A. *Phys. Rev.* **1974**, *B17*, 4246.
(5) Hoefdraad, H. E.; Blasse, G. *Phys. Stat. Sol.* **1975**, *A 29*, K95.
(6) Piper, W. W.; DeLuca, J. A.; Ham, F. S. *J. Lumin.* **1974**, *8*, 344.
(7) Sommerdijik, J. L.; Bril, A.; de Jager, A. W. *J. Lumin.* **1974**, *8*, 341.
(8) Sommerdijik, J. L.; Bril, A.; de Jager, A. W. *J. Lumin.* **1974**, 9, 288.

10.1021/cm050394z CCC: $30.25
Published on Web 05/10/2005

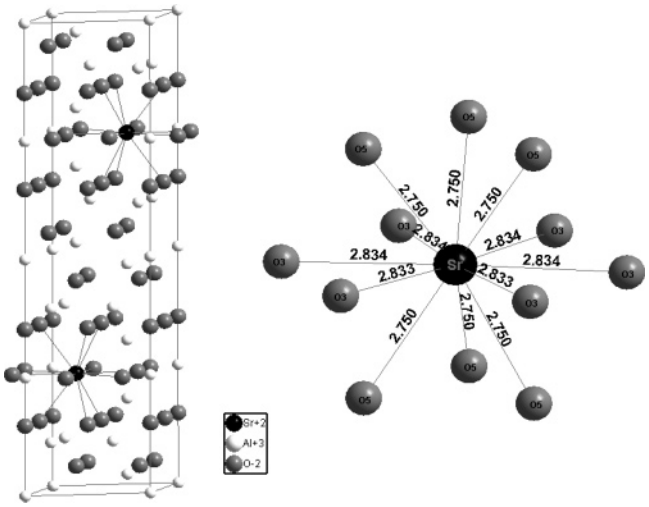

Figure 2. Structural model (left) and Sr coordination polyhedra (right) for $SrAl_{12}O_{19}$ hexagonal magnetoplumbite.

under 185-nm excitation. High QEs have also been reported for other fluoride-based Pr^{3+}-doped host lattices.[9−11]

QS has also been observed in oxide materials such as $SrAl_{12}O_{19}$,[12] $LaMgB_5O_{10}$,[13] LaB_3O_6,[14] and SrB_4O_7.[15]

$SrAl_{12}O_{19}$ adopts a hexagonal magnetoplumbite structure, crystallizing in space group $P6_3/mmc$. In this lattice, Pr^{3+} substitutes for Sr^{2+} with charge compensation from Mg^{2+} substituting for Al^{3+} in the spinel block of the structure. The high coordination number (12) for the Sr^{2+} ion as well as the relatively long Sr−O bond distances ($6 \times \sim 2.75$Å $+ 6 \times \sim 2.785$Å)[16] (see Figure 2) results in a weak crystal field and small centroid shift, satisfying the desired crystal structure requirements for Pr^{3+} QS.

Materials synthesized at the nanoscale have been known to display novel physical properties due to quantum confinement.[17] This is especially true in the case of semiconductor materials such as CdTe or CdSe, for which well-established synthetic procedures are able to achieve careful size control at the nanoscale.[18] In ionic materials, including the oxides investigated in this paper, confinement plays a negligible role due to small Bohr radius of the exciton.

The present investigation of QS in *nanoparticles* of $SrAl_{12}O_{19}$:Pr^{3+} was motivated by the observation that the quantum efficiency of oxide materials fabricated in the nanosize regime is usually lower when compared to micrometer-sized particles due to surface effects.[19−26] In such cases, the relatively high surface-to-volume ratio plays an important role and segregation may cause reduced efficiency due to unfavorable coordination environment of the dopants necessary for optical activation. In addition, strong quenching of the luminescent ions through coupling with high-frequency surface −OH or −COOH groups can also occur.[27] Furthermore, the processing methods necessary to produce well-ordered oxide crystalline lattices generally involve processing at high temperatures, which tend to agglomerate the primary crystallites, and thus lose the possible benefits of a nanosize material.

Therefore, preserving the QS effect and (more importantly) its efficiency in nanocrystalline materials requires careful synthesis in order to stabilize the nanocrystallites of a complex oxide host lattice while not perturbing the local environment surrounding the doping ion. The main goal of this paper is to demonstrate the first synthesis of high quality nanocrystallites of the quantum splitting phosphor $SrAl_{12}O_{19}$:1% Pr, Mg. The synthesized nanocrystalline phosphors have been carefully characterized by X-ray diffraction (XRD), transmission electron microscopy (TEM), electron energy loss spectroscopy (EELS), emission, photoexcitation, and time-resolved fluorescence measurements. We demonstrate that the nanocrystalline material shows no physical property degradation and that the quantum splitting properties of the material are retained in the nanocrystalline particles.

Experimental Section

A batch of $SrAl_{12}O_{19}$:1% Pr, Mg was prepared by dissolving stoichiometric amounts of $Sr(NO_3)_2$ (Alfa Aesar 99.97%), $Al(NO_3)_3 \cdot 9H_2O$ (Alfa Aesar 99.999%), $Pr(NO_3)_3 \cdot 6H_2O$ (Alfa Aesar 99.99%), and $Mg(NO_3)_2 \cdot 6H_2O$ (Alfa Aesar 99.97%), in 100 cm^3 of deionized water under constant stirring for 1 h and subsequent addition of a 5 wt % poly(vinyl alcohol) (Aldrich, 99+% hydrolyzed 115 000 MW) solution.[28] The resulting mixed solution was precipitated by dropwise addition of 100 cm^3 of NH_4OH (28−30%) solution. The obtained material dried in an IR oven for 24 h and calcined at temperatures between 400 and 1400 °C for 4−40 h under air. At each calcination step, a small aliquot of the sample was removed and characterized by X-ray powder diffraction. Microcrystalline $SrAl_{12}O_{19}$:1% Pr, Mg phosphors were synthesized by conventional solid-state reactions of stoichiometric mixtures of $SrCO_3$, Al_2O_3, Pr_6O_{11}, and MgO that were fired between 1300 and 1500 °C under reducing atmospheres.

The X-ray powder diffraction was performed using two Bruker D8 Advance diffractometers. The first used Ni-filtered Cu Kα radiation and a scintillation detector with fixed slits of 1/1/0.1 mm for the aperture, scattered-radiation, and detector slits, respectively.

(9) van der Kolk, E.; Dorenbos, P.; van Eijk, C. W. E. *Optics Commun.* **2001**, *197*, 317.
(10) Sokólska, I.; Kück, S. *Chem. Phys.* **2001**, *270*, 355.
(11) Kück, S.; Sokólska, I.; Henke, M.; Döring, M.; Scheffler, T. *J. Lumin.* **2003**, *176*, 102.
(12) Srivastava, A. M.; Beers, W. W. *J. Lumin.* **1997**, *71*, 285.
(13) Srivastava, A. M.; Doughty, D. A.; Beers, W. W. *J. Electrochem. Soc.* **1996**, *143*, 4113.
(14) Srivastava, A. M.; Doughty, D. A.; Beers, W. W. *J. Electrochem. Soc.* **1997**, *144*, 190.
(15) Yang, Z., et al. *Acta Chim. Sin.* **2001**, *59*, 1372.
(16) Lindop, A. J.; Matthews, C.; Goodwin, D. W. *Acta Crystallogr.* **1975**, *B31*, 2940.
(17) Alivisatos, A. P. *J. Phys. Chem.* **1996**, *100*, 13226.
(18) Donega, C. D.; Hickey, S. G.; Wuister, S. F.; Vanmaekelbergh, D.; Meijerink, A. *J. Phys. Chem.* **2003**, *B107*, 409.
(19) Trojan-Piegza, J., et al. *J. Alloys Compd.* **2004**, *380*, 123.
(20) Riwotzki, K.; Haase, M. *J. Phys. Chem. B* **1998**, *102*, 10129−10135.
(21) Riwotzki, K.; Meyssamy, H.; Kornowski, A.; Haase, M. *J. Phys. Chem. B* **2000**, *104*, 2824−2828.
(22) Schmechel, R.; Kennedy, M.; von Seggern, H.; Winkler, H.; Kolbe, M.; A Fischer, R.; Xaomao, L.; Benker, A.; Winterer, M.; Hahn, H. *J. Appl. Phys.* **2001**, *89*, 3, 1679−1686.
(23) Riwotzki, K.; Haase, M. *J. Phys. Chem. B* **2001**, *105*, 12709−12713.
(24) Feldman, C. *Adv. Funct. Mater.* **2003**, *13*, 2, 101−107.
(25) Wei, Z.-G.; Sun, L.-D.; Jiang, X.-C.; Liao, C.-S.; Yan, C.-H. *Chem. Mater.* **2003**, *15*, 3011−3017.
(26) Kömper, K.; Borchert, H.; Storz, J.; Lobo, A.; Adam, S.; Möller, T.; Haase, M. *Angew. Chem., Int. Ed.*, **2003**, *42*, 5513−5516.
(27) Krebs, J. K.; Feofilov, S. P.; Kaplyanskii, A. A.; Zakharchenia, R. I.; Happek, U. *J. Lumin.* **1999**, *83*, 209.
(28) Kriven, W. M.; Lee, S. J.; Gulgun, M. A.; Nguyen, M. H.; Kim, D. K. *Ceram. Trans.* **2000**, *108*, 99.

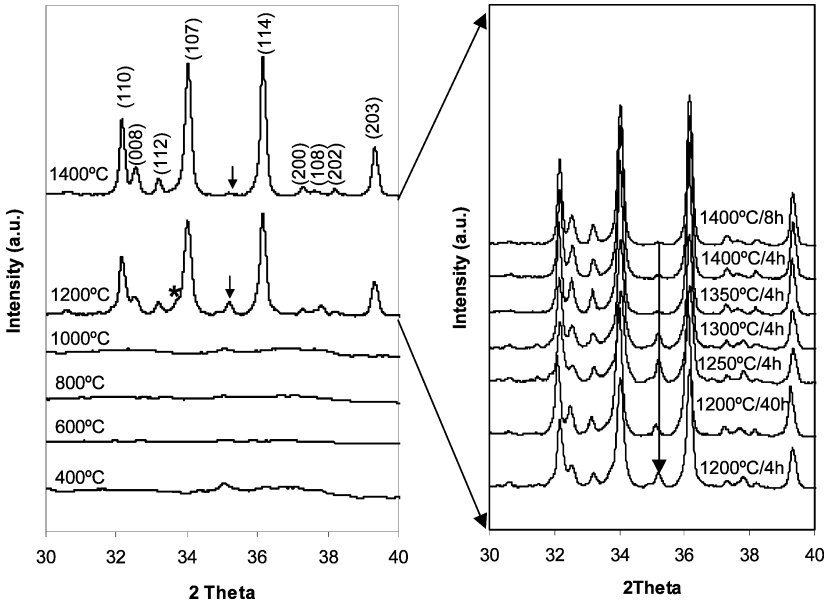

Figure 3. XRD spectra for $SrAl_{12}O_{19}$:1% Pr, Mg samples synthesized at temperatures between 400 and 1400 °C for 4 h (left) and at additional calcination conditions (right). The arrows indicate the reflection of nanosized Al_2O_3. The asterisk indicates unreacted $SrAl_4O_7$.

The instrument was operated in $\theta-2\theta$ geometry within the 30−40° region, with a step size of 0.02, and 5 s/step. Diffraction patterns were also collected over the same angular range using a $\theta-\theta$ Bruker D8 Advance diffractometer equipped with a linear position-sensitive detector (PSD-50m) manufactured by M. Braun. Ni-filtered Cu Kα radiation was used with an aperture slit of 0.6 mm. For each instrument, NIST-certified SRM 660a LaB_6 was used to determine the instrumental contributions to the diffraction peak broadening. An estimate of the average crystallite size was obtained using the Scherrer equation.

The TEM was carried out using a 200-keV field-emission microscope (FEI Tecnai F20) equipped with high-resolution TEM, energy-dispersive spectrometry, and EELS capabilities. The particles were suspended in methanol, sonicated, and then dispersed onto a thin holey-carbon support film for TEM analysis. Chemical composition was evaluated using energy-dispersive X-ray spectroscopy, typically performed on an individual particle using a focused electron probe.

Emission spectra were measured using samples pressed into an aluminum mount, covered with a UV-grade fused quartz window, and mounted in a temperature variable optical cryostat (Oxford Instruments). The samples were excited with an MPB PSX-100 compact ArF excimer laser at $\lambda = 193$ nm, which coincides with the peak of the f−d absorption band. The emission was collected with a concave mirror and recorded with a UV-enhanced Princeton Instrument liquid nitrogen cooled charge-coupled device, mounted to a 0.275-m Acton Research grating monochromator with a 150 g/mm grating, blazed at 300 nm. Stray light from the 193-nm excitation was removed with a nonfluorescent liquid filter (cutoff $\lambda = 200$ nm). For wavelengths above 380 nm, a Schott WG345 long-pass filter was inserted to remove second-order diffraction signals. The relative quantum efficiency of the detection system (including collection optics, filters, and cryostat windows) was calibrated in the spectral range between 200 and 500 nm with a tunable light source by comparing the detection system response to the light source photon flux as determined using a NIST-traceable calibrated Hamamatsu photodiode. For relaxation measurements of the Pr^{3+} $^1S_0$ level, radiation from the short-pulse MPB PSX-100 ArF excimer laser (pulse duration 2.5 ns) was used to excite the samples. By use of the same sample mount, cryostat, filters, and collection optics as for the emission spectra measurements, the transient luminescence of the $^1S_0$ to $^1I_6$ transition was observed. The luminescence was filtered with a Jarrell Ash 0.25-m monochromator tuned to $\lambda = 405$ nm. The luminescence was detected using a Hamamatsu R212 photomultiplier and recorded with a Stanford Instruments multichannel scaler. For photoexcitation measurements in the UV spectral region, the samples were pressed into a windowless aluminum mount, and a sodium salicylate sample was used to calibrate the photon flux of the excitation source. The sample mount was inserted into a vacuum sample chamber, which was attached to a 0.2-m McPherson 302 VUV monochromator, equipped with a Hamamatsu deuterium lamp as the excitation source. The sample chamber was separated from the VUV monochromator via a VUV MgF_2 window, and the radiation was focused with an Al-coated spherical mirror onto the samples at normal incidence. Luminescence was collected with a short focal length off-axis parabolic mirror mounted in front of the sample, with a central hole in the parabolic mirror to allow optical excitation of the samples. The luminescence was transmitted through a UV-grade quartz window onto a Hamamatsu R212 photomultiplier. An interference filter was used to select radiation from the $^1S_0$ to $^1I_6$ transition at 275 nm. A nonfluorescence liquid filter (cutoff wavelength 200 nm) was inserted in front of the interference filter to avoid spurious fluorescence from the interference filter substrate. The fluorescence as a function of excitation wavelength was recorded with a FAST-Comtech multichannel scaler and normalized to the incident photon flux as obtained form the sodium salicylate signal.

Results and Discussion

Upon calcination at 400 °C for 4 h, the $SrAl_{12}O_{19}$:1% Pr, Mg sample showed macroscopically gray areas due to incomplete organic matter decomposition. The sample was subsequently heated at 450, 500, and 550 °C for similar duration and atmosphere. Since macroscopic inhomogeneities still persisted, the sample was removed and milled under 2-propanol using high-density/high-purity Al_2O_3 grinding media for 6 h and subsequently calcined at 600°C for additional 4 h under air. Upon completion of this step, the batch showed no visible grayness and was completely white. The X-ray powder diffraction shows absence of reflections

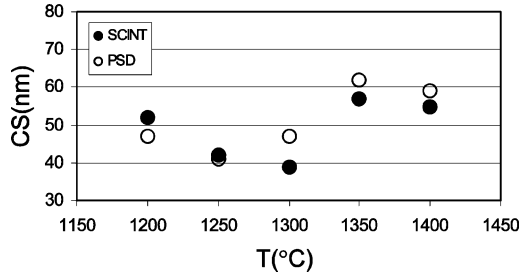

Figure 4. Crystallite size of $SrAl_{12}O_{19}$:1% Pr, Mg phases calcined at different temperatures during 4 h and measured using a scintillation and position-sensitive detector.

belonging to Sr−Al−O phases up to 1000 °C, indicating a mostly amorphous material (Figure 3).

At 1200 °C/4 h, the X-ray powder diffraction shows that reflections belonging to the desired $SrAl_{12}O_{19}$:1% Pr, Mg phase are detected. A small amount of unreacted $SrAl_4O_7$ and nanosized Al_2O_3 (signaled by the arrows in Figure 3) still remain in the sample. Increasing the temperature to 1400 °C/4 h considerably increases the proportion of the $SrAl_{12}O_{19}$:1% Pr, Mg phase, and a nearly single phase sample is obtained.

The average crystallite size was carefully verified on samples synthesized under several calcination conditions using both scintillation and position-sensitive detectors and the Scherrer equation. Because of the low dopant levels, no significant lattice strain is expected, and the Scherrer equation provides reasonable crystallite size estimation. It should be noted that the estimate of the crystallite size is volume averaged in the direction perpendicular to the plane of diffraction and therefore provides no information about the nanocrystallite size distribution.

Because of the hexagonal crystal structure, the nanocrystallites tend to adopt anisotropic platelike morphologies. As evidence for anisotropy in the X-ray diffraction patterns, it can be seen that the (114) peak is clearly sharper than the (107) peak, indicating larger sizes in the ⟨110⟩ direction that are found to be outside of the reliable nanoregime that can be estimated using the Scherrer equation. Profile fitting of a (0,0,*l*) reflection would be the preferred choice to estimate the thickness of the crystallites using X-ray diffraction. However, the same platelike nature of the crystallites causes the (0,0,*l*) reflections to be generally weak in intensity (in addition to the fact that they are sometimes convoluted with other reflections). As such, they are less than ideal for crystallite thickness estimation. Thus, the (107) peak was used for size determinations as the ⟨107⟩ direction closely approximates the ⟨001⟩ direction. Taking into account the above-mentioned considerations, we have verified that the different combinations of final calcination temperatures and times yield materials with primary crystallite thickness comprised between ∼40 and 65 nm (see Figure 4 for samples calcined at different temperatures for 4 h).

TEM images showed well-defined platelet crystallites with crystallite size in the planar ⟨110⟩ direction ranging from 60 to 300 nm (see Figure 5). High-resolution electron microscopy used to assess crystallinity near the particle surface(s) showed no evidence of near-surface amorphization in the $SrAl_{12}O_{19}$:1% Pr, Mg nanocrystallites. Particle thickness was evaluated using the low-loss portion of the energy-loss

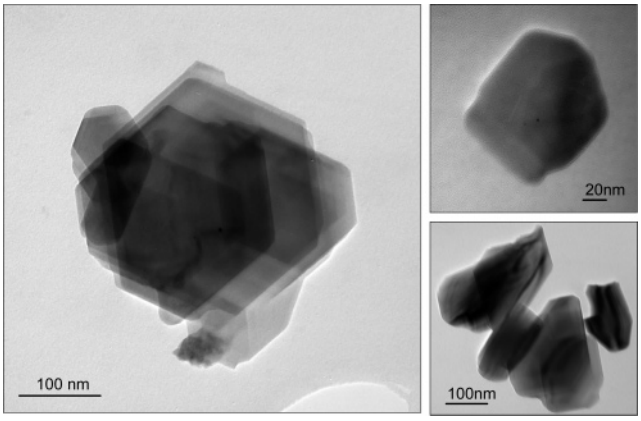

Figure 5. TEM of a $SrAl_{12}O_{19}$:1% Pr, Mg sample showing well-defined nanocrystallites.

spectrum to measure the relative intensities of elastic and inelastic scattering. In this technique, absolute particle thickness can be determined from the scattering profile, when the inelastic mean free path (λ_{in}) of a 200-keV electron is known for the material of interest. Although a precise value of λ_{in} is not known for the $SrAl_{12}O_{19}$:1% Pr, Mg phase, we approximate this value as 100−140 nm based on known λ_{in} values for other metal oxide systems.[29] By use of this approach, individual particle thickness is calculated to be 30−35 nm. We have also evaluated the thickness of several agglomerates of $SrAl_{12}O_{19}$:1% Pr, Mg nanocrystallites found stacked together as seen in Figure 5, which vary between ∼50 and 80 nm. This correlates well with the XRD values, which indicate a primary crystallite size comprised between ∼30 and 60 nm.

Figure 6 shows the normalized and corrected luminescence spectra of the nanocrystalline and microcrystalline (insert) $SrAl_{12}O_{19}$:1% Pr, Mg samples at 10 (bottom) and 290 K (top). A comparison between the emission spectrum for the nanocrystalline sample and that of the microcrystalline material shows that the branching ratios for the $^1S_0$ relaxation at low temperatures and room temperature are statistically identical. The emission lines at 215, 255, 275, 345, and 405 nm are assigned to optical transitions from the $^1S_0$ to the $^3H_4$, $^3F_2$, $^3G_4$, $^1D_2$, and $^1I_6$, respectively. The $^1S_0$ to $^1I_6$ emission and the $^3P_0$ emission at 490 nm constitute the quantum cascade process in this system. A careful comparison shows that the $^1S_0$ to $^1I_6$ transition in the nanocrystalline sample is slightly enhanced, when compared to the microcrystalline sample. The emission spectra not only confirm the preservation of the bulk branching ratio in a 50-nm particle but more importantly demonstrate the absence of impurity or surface-induced loss mechanisms which have been reported for other nanocrystalline systems.

We have evaluated the efficiency of our high quality nanocrystalline $SrAl_{12}O_{19}$:1% Pr, Mg by comparing the radiative lifetime of the $^1S_0$ emission in both nanocrystalline and microcrystalline $SrAl_{12}O_{19}$:1% Pr, Mg samples. Figure 7 shows a typical relaxation curve of the $^1S_0$ to $^1I_6$ transition of nanocrystalline sample recorded at 10 K (the detection wavelength is 405 nm). The relaxation can be fit using a single-exponential decay with a relaxation time of 595 ± 5

(29) Egerton, R. F.; Cheng, S. C. *Ultramicroscopy* **1987**, *21*, 3, 231.

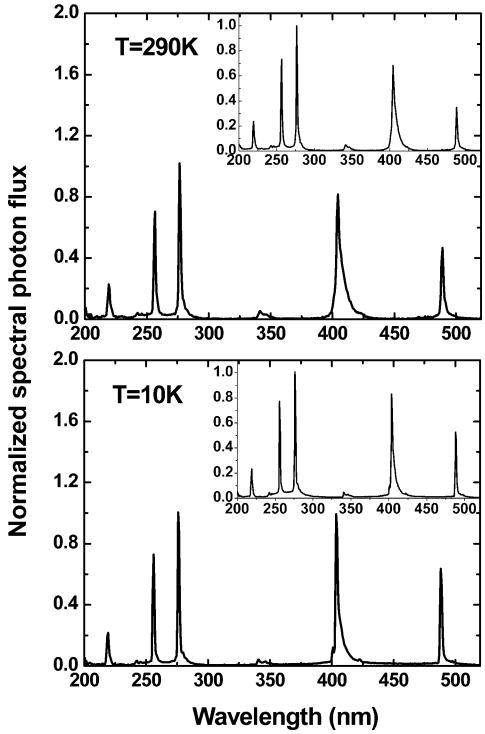

Figure 6. Emission spectra for nanocrystalline and microcrystalline (insert) $SrAl_{12}O_{19}$:1% Pr, Mg at 10 (bottom) and 290 K (top).

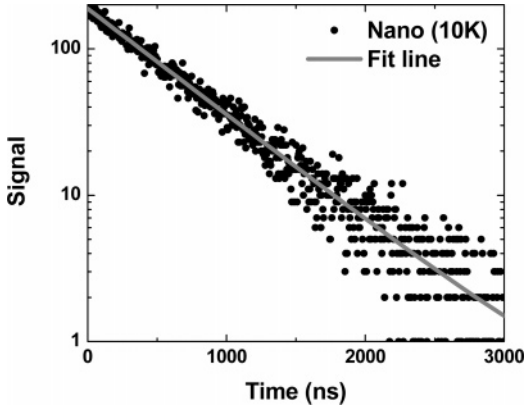

Figure 7. Time-resolved fluorescence for the nanocrystalline $SrAl_{12}O_{19}$:1% Pr, Mg at 10 K after pulsed excitation at 193 nm. The detection wavelength is 405 nm.

ns. The relaxation times for the nanocrystalline sample are about 5% shorter than those for the microcrystalline sample. We note that the $^1S_0$ relaxation times are exceptionally fast for a parity-forbidden transition. This is due to mixing with the nearby 4f5d state, leading to relaxation of the parity selection rule.

In comparison, systems such as $CePO_4$:Tb, $LaPO_4$:Eu^{3+}, and YVO_4:Eu^{3+} with strongly reduced quantum efficiency and/or nonexponential relaxation curves are observed and generally attributed to energy migration to the nanoparticle surface and subsequent quenching due to surface ions.[19−26]

Figure 8 shows the $^1S_0$ relaxation time as a function of temperature for both samples. The samples show a similar temperature dependence of the relaxation time, i.e., a nearly temperature-independent lifetime at temperature below 200 K, and a weak onset of temperature quenching at higher temperatures. The time-resolved measurements of the nanocrystalline samples show that there are virtually no additional

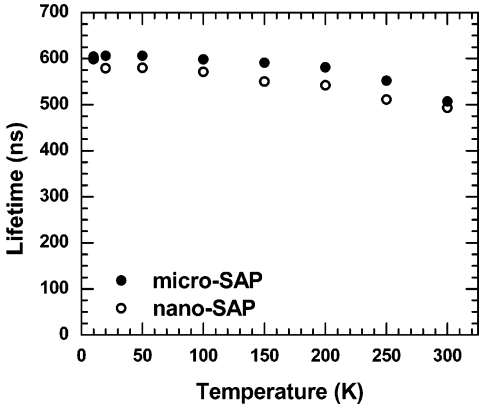

Figure 8. Temperature dependence of the $^1S_0$ relaxation time for the nanocrystalline (open circles) and microcrystalline $SrAl_{12}O_{19}$:1% Pr, Mg (solid dots). Detection wavelength: 405 nm.

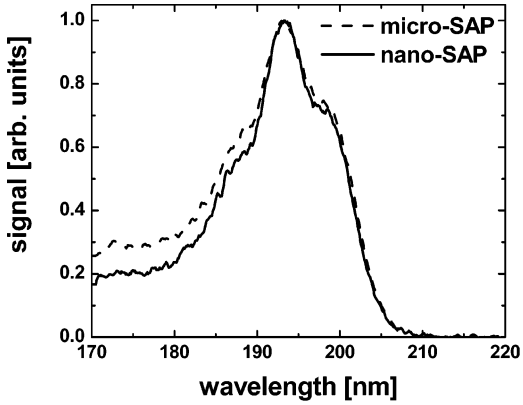

Figure 9. Excitation spectra of nanocrystalline (solid line) and microcrystalline (dashed line) $SrAl_{12}O_{19}$:1% Pr, Mg. The detection wavelength is 275 nm.

quenching processes in the nanocrystalline samples compared to the bulk samples. In combination with the excitation and emission measurements, this is further evidence of the high quality of these nanoparticles.

Figure 9 shows the excitation spectra of the nano- and microcrystalline $SrAl_{12}O_{19}$:1% Pr, Mg at room-temperature normalized to the signal maxima. Once more, we find very similar spectra for the two samples, dominated by the f−d transitions of the Pr^{3+} ion. A recent analysis of the relationship between the energy position of the Ce^{3+} and Pr^{3+} 4f5d states in 64 different compounds yields the aforementioned energy difference of 12 240 ± 750 cm^{-1}.[30] The five crystal-field levels of the Ce^{3+} 5d state have been identified in the excitation spectrum of $SrAl_{12}O_{19}$:Ce^{3+}. The corresponding crystal field components of the Pr^{3+} 5d state in $SrAl_{12}O_{19}$ can be identified using the relationship $E_{Pr} = 12\,240\ cm^{-1} + E_{Ce}$. The resulting (theoretical) splitting pattern places the peaks in the excitation spectrum at 198 nm (50 554 cm^{-1}), 193 nm (51 920 cm^{-1}), 189 nm (53 225 cm^{-1}), 183 nm (54 790 cm^{-1}), and 176 nm (56 883 cm^{-1}). The anticipated splitting pattern is very consistent with the observed splitting in the excitation spectrum (Figure 9). The total crystal field splitting is thus approximately 6 300 cm^{-1}.

Thus, the optical measurements show that no new features in the nanocrystalline phase and the observed small differ-

(30) Dorenbos, P. *J. Lumin.* **2000**, *91*, 155.

ences from the microcrystalline material are well within the range of variations found in microcrystalline materials synthesized under different conditions.

We attribute the fact that the quantum efficiencies displayed by our nanopowders are comparable to those of micrometer-sized powders to two concomitant reasons: the synthesis procedure that yielded high-crystallinity nanopowders that resulted in the absence of additional quenching effects generally observed in other rare earth doped large band gap luminescent nanoparticles; and the rapid relaxation of the praseodymium $1S_0$ state ($\tau = 600$ ns) compared to that of trivalent europium and terbium, which exhibit relaxation times on the order of several milliseconds.

Conclusions

We have reported on the first observation of quantum splitting effect in $SrAl_{12}O_{19}$:1% Pr, Mg nanocrystalline powders synthesized using a surfactant-mediated processing route that could be easily adopted for large-scale production of nanomaterials. We have carried out microstructural, emission, photoexcitation, and time-resolved fluorescence studies on the synthesized materials and verified that the temperature dependence features and branching ratios for the $^1S_0$ relaxation at low temperatures and room temperature are maintained at the nanoscale and that no property degradation due to impurity or surface-induced loss mechanisms commonly reported for other nanocrystalline systems was found.

Acknowledgment. This report was prepared with the support of the U.S. Department of Energy, under Award No. DE-FC26-03NT4295. However, any opinions, findings, conclusions, or recommendations expressed herein are those of the author(s) and do not necessarily reflect the views of the Department of Energy.

CM050394Z